Monthly Notices of the ROYAL ASTRONOMICAL SOCIETY
MNRAS **457,** 258–266 (2016) doi:10.1093/mnras/stv2849

NuSTAR discovery of a cyclotron absorption line in the transient X-ray pulsar 2S 1553−542

Sergey S. Tsygankov,[1⋆] Alexander A. Lutovinov,[2] Roman A. Krivonos,[2] Sergey V. Molkov,[2] Peter J. Jenke,[3] Mark H. Finger[4] and Juri Poutanen[1,5]

[1]*Tuorla Observatory, Department of Physics and Astronomy, University of Turku, Väisäläntie 20, FI-21500 Piikkiö, Finland*
[2]*Space Research Institute of the Russian Academy of Sciences, Profsoyuznaya Str. 84/32, Moscow 117997, Russia*
[3]*University of Alabama in Huntsville, 301 Sparkman Drive, Huntsville, AL 35899, USA*
[4]*Universities Space Research Association, National Space Science and Technology Center, 320 Sparkman Drive, Huntsville, AL 35805, USA*
[5]*Nordita, KTH Royal Institute of Technology and Stockholm University, Roslagstullsbacken 23, SE-10691 Stockholm, Sweden*

Accepted 2015 December 2. Received 2015 November 26; in original form 2015 September 19

ABSTRACT

We report the results of a spectral and timing analysis of the poorly studied transient X-ray pulsar 2S 1553−542 using data collected with the *NuSTAR* and *Chandra* observatories and the *Fermi*/GBM instrument during an outburst in 2015. The properties of the source at high energies (>30 keV) are studied for the first time and the sky position has been essentially improved. The source broad-band spectrum has a quite complicated shape and can be reasonably described by a composite model with two continuum components – a blackbody emission with the temperature about 1 keV at low energies and a power law with an exponential cut-off at high energies. Additionally, an absorption feature at ∼23.5 keV is discovered both in phase-averaged and phase-resolved spectra and interpreted as the cyclotron resonance scattering feature corresponding to the magnetic field strength of the neutron star $B \sim 3 \times 10^{12}$ G. Based on the *Fermi*/GBM data, the orbital parameters of the system were substantially improved, which allowed us to determine the spin period of the neutron star $P = 9.27880(3)$ s and a local spin-up $\dot{P} \simeq -7.5 \times 10^{-10}$ s s^{-1} due to the mass accretion during the *NuSTAR* observations. Assuming accretion from the disc and using standard torque models, we estimated the distance to the system as $d = 20 \pm 4$ kpc.

Key words: accretion, accretion discs – magnetic fields – stars: individual: 2S 1553−542 – X-rays: binaries.

1 INTRODUCTION

The transient source 2S 1553−542 belongs to the numerous subclass of the accreting X-ray pulsars with Be optical companions (BeXRP). It was discovered by the *SAS-3* observatory during the Galactic plane survey in 1975 (Walter 1976). Later, the transient nature of the source was established as well as strong pulsations with a period of 9.3 s and amplitude of ∼80 per cent (Kelley, Ayasli & Rappaport 1982). Using the same data, the orbital period of the binary system was measured as $P_{\rm orb} = 30.6 \pm 2.2$ d and a suggestion that 2S 1553−542 is likely a Be/X-ray binary system has been made (Kelley, Rappaport & Ayasli 1983). Note that no optical counterpart has directly been determined for 2S 1553−542 so far (however, see below).

The second time after its discovery that 2S 1553−542 came into the view of X-ray instruments was during the outburst in 2007–2008 (Krimm et al. 2007). An intensive monitoring of this outburst with the *RXTE* observatory allowed us to improve the orbital parameters of the system and to trace the spectral evolution in the energy range 2.5–30 keV (Pahari & Pal 2012). In particular, it was shown that the source spectra in all available intensity states can be fitted well with the combination of a blackbody component (with temperature varying between 2.5 and 4 keV) and a broken power-law component. The iron emission line at ∼6.5 keV and a strong photoelectric absorption corresponding to a hydrogen column density of $N_{\rm H} \sim 5 \times 10^{22}$ cm^{-2} were also required by the fit.

The third episode when 2S 1553−542 underwent an outburst was observed in the beginning of 2015. The increase of the flux seen in the *MAXI*/GSC data was reported by Sugizaki et al. (2015). The estimated starting date of the activity was around 2015 January 28 (MJD 57 050).

⋆E-mail: stsygankov@gmail.com

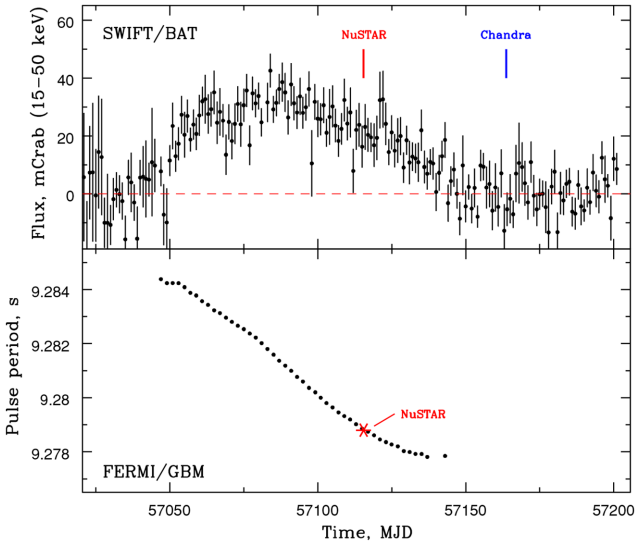

Figure 1. Top: *Swift*/BAT light curve of 2S 1553−542 in the 15–50 keV energy band (black points). Flux is given in units of mCrab (1 mCrab = 1.4×10^{-11} erg s^{-1} cm^{-2}). The times of the *NuSTAR* and *Chandra* observations are marked. Bottom: Evolution of the pulsar spin period over the outburst as seen by the *Fermi* Gamma-Ray Burst Monitor (GBM). The asterisk shows the period measured by *NuSTAR* corrected for the orbital motion (see text for details).

In this paper, we describe the results of the comprehensive spectral and temporal analysis of the high-quality data collected by the *NuSTAR* observatory during the declining phase of this outburst (MJD 57 115.48). The main goal was to explore the source properties at high energies (above 30 keV) for the first time.

2 OBSERVATIONS AND DATA REDUCTION

2.1 *NuSTAR* observations

The *Nuclear Spectroscopic Telescope Array (NuSTAR)* (Harrison et al. 2013), launched on 2012 June 13, is the first orbital X-ray focusing telescope operating at energies above 10 keV. The observatory consists of two co-aligned identical X-ray telescope systems operating in a wide energy range from 3 to 79 keV with angular resolution of 18 arcsec (full width at half-maximum or FWHM) and half-power diameter of 58 arcsec. A spectral energy resolution of 400 eV (FWHM) at 10 keV is provided by independent solid-state CdZnTe pixel detector units for each telescope, usually referred to as focal plane modules A and B (FPMA and FPMB).

NuSTAR performed a TOO observation of 2S 1553−542 in the declining phase of the outburst (MJD 57 115.4834, see Fig. 1) with a total exposure time of 27 ks (observation ID 90101002002). The source was relatively bright, demonstrating a net count rate of about 20 cts s^{-1} on both FPMA and FPMB. We did not notice any special issues related to the high count rate of the source in the following analysis. The source covered a large area in the field of view (Fig. 2) because the *NuSTAR* point spread function has wide wings (Harrison et al. 2013; An et al. 2014). The data were reduced using the NuSTARDAS pipeline version v1.4.1 (2014 May 28) and CALDB version 20150612.

To perform barycentric corrections, it is necessary to know the source position to good accuracy. Observations with the *Chandra* observatory, performed on 2015 May 21 (MJD 57 163.68; observation ID 17662), allowed us to measure it as RA = $15^{\rm h}57^{\rm m}48\overset{\rm s}{.}3$,

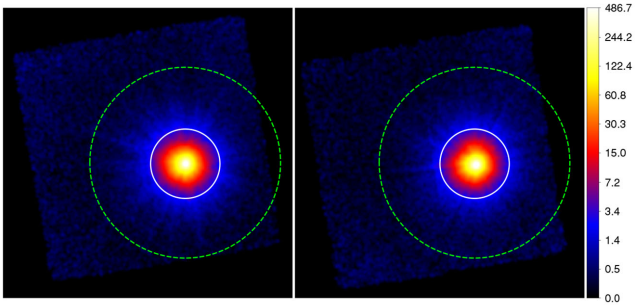

Figure 2. Exposure-corrected sky images of 2S 1553−542 from FPMA (left) and FPMB (right) in the 3–79 keV energy band. The images have been smoothed by a Gaussian kernel with 9 arcsec width and colour-coded in logarithmic scale for convenience. The colour bar on the right indicates the units of the images expressed in 10^{-4} cts pix^{-1} s^{-1}. The solid white circle (120 arcsec radius) denotes the region for the source extraction. The NUSKYBGD background model has been calibrated in the area outside the green dashed circle (330 arcsec radius).

Dec = $-54^\circ24'53\overset{''}{.}1$ (J2000) with a $1''$ uncertainty (90 per cent). Note that these *Chandra* observations as well as observations with the *Swift*/XRT telescope were used to determine the optical counterpart in the system and to measure the absorption value (Lutovinov et al. 2015b). The latter is important for the analysis of the *NuSTAR* data as it works above 3 keV and is not very sensitive to the small or moderate absorption values. Recall that a quite high photoabsorption ($4–5 \times 10^{22}$ cm^{-2}) was required by Pahari & Pal (2012) to describe the source spectra, obtained with the *RXTE* observatory (it also operates above 3 keV). Such high values are quite atypical for BeXRPs, whose spectra do not usually demonstrate strong absorption. Our analysis of *Chandra* and *Swift*/XRT data in the soft X-ray band shows a lower photoabsorption value in the source spectrum, around $\simeq 2.3 \times 10^{22}$ cm^{-2} (Lutovinov et al. 2015b), which was fixed in the following spectral analysis of the *NuSTAR* data. Note that it is only slightly higher than the estimations of the Galactic interstellar absorption in this direction, $\sim 1.6–1.9 \times 10^{22}$ cm^{-2} (Dickey & Lockman 1990; Kalberla et al. 2005).

We extracted spectra using the NUPRODUCTS script provided by the NuSTARDAS pipeline. The source spectrum was extracted within the 120 arcsec aperture around the source position as shown in Fig. 2, which constitutes 92 per cent of the enclosed energy of the point spread function (see e.g., An et al. 2014). The *NuSTAR* background varies across the field of view due to the different stray light (also called aperture) background components: individual bright X-ray sources, isotropic extragalactic cosmic X-ray background (CXB) and Galactic ridge X-ray emission (GRXE) (Wik et al. 2014). The field around 2S 1553−542 does not contain stray light from nearby Galactic sources, but it has CXB and GRXE components in the background, because 2S 1553−542 is located in the Galactic plane ($l^{II} = -32.056$ and $b^{II} = -0.857$). We used a suite of IDL routines NUSKYBGD (Wik et al. 2014) to model all the known background components (instrumental, CXB and GRXE) in the source-free region outside the green dashed circle ($R = 330$ arcsec) shown in Fig. 2. This model was utilized to estimate the background spectrum at the position of the source.

2.2 *Fermi*/GBM and *Swift*/Burst Alert Telescope observations

Fermi Gamma-Ray Burst Monitor (GBM) is an all sky monitor whose primary objective is to extend the energy range over which gamma-ray bursts are observed in the Large Area Telescope on

Fermi (Meegan et al. 2009). GBM consists of 12 NaI detectors with a diameter of 12.7 cm and a thickness of 1.27 cm and two BGO detectors with a diameter and thickness of 12.7 cm. The NaI detectors have an energy range from 8 keV to 1 MeV while the BGOs extend the energy range to 40 MeV.

The *Swift* Burst Alert Telescope (BAT) is a hard X-ray monitor that has a field of view of 1.4 sr and its array of CdZnTe detectors are sensitive in the 15–150 keV range (Krimm et al. 2013). It is a coded aperture instrument with a detector area of 5200 cm^2. We use the BAT transient monitor results[1] (15–50 keV), provided by the BAT team, to model the torque imparted to the neutron star by the accreted material.

GBM channel 1 (12–25 keV) CTIME data from 57 020 to 57 145 MJD is binned to 250 ms and fit to a semi-empirical background model. The background model is subtracted and pulsed flux and frequencies for 2S 1553−542 are extracted from the data by modelling its Fourier components (Finger et al. 1999; Jenke et al. 2012).

3 RESULTS

As can be seen from Fig. 1 (top), the total duration of the analysed outburst is around 3.5 months covering more than three complete binary orbital cycles. Such a duration is typical for type II outbursts from BeXRPs. These events are caused by the non-stationary increase of the amount of matter in the Be circumstellar disc. Peak luminosities can be much higher than 10^{37} erg s^{-1} (for a review, see Reig 2011).

3.1 Orbital parameters

We determined an orbital model for 2S 1553−542 using the *Fermi*/GBM and the *Swift*/BAT data. Typically, after correcting the pulse arrival times for Earth's motion, one can use the Doppler-boosted frequencies of the pulses to fit a model for the binary system. Material accreted on to a neutron star surface or collected in an accretion disc threaded by the neutron star's magnetic field transfers angular momentum to the neutron star. Disentangling this intrinsic spin-up from the orbital signature is challenging. A solution to this problem is to model the intrinsic spin-up using a proxy for the system's X-ray luminosity. The luminosity is a function of mass accretion, which is related to the torque imposed on the neutron star. Rappaport & Joss (1977) showed that, at high luminosity, the intrinsic spin-up, $\dot{\nu}$, is proportional to $L^{6/7}$ when accretion is mediated through a disc. The proportionality constant is a function of mass, radius, moment of inertia, distance and magnetic field of the neutron star along with a few parameters describing accretion and emission efficiency. When connecting multiple outbursts with the same torque model, it is necessary to include a spin-down term to account for angular momentum losses during quiescence.

A search for frequency and frequency rate is performed using pulse profiles from GBM folded over a 2-day interval. Each frequency epoch is chosen as the mean exposure-weighted observation time. The epochs are barycentred using the JPL Planetary ephemeris DE200 (Standish 1990). BAT survey data (15–50 keV) for 2S 1553−542 are used as a proxy for the source luminosity and to model the intrinsic spin-up rate. To eliminate under-constrained and over-constrained rates, only BAT rates with errors greater than 10^{-3} and less than 0.05 are used. This spin-up model along with the line-of-sight delay associated with the binary orbit from Deeter, Boynton & Pravdo (1981) is used to model the barycentred arrival times. Minimization of the χ^2 fit of the barycentric frequencies and the BAT rates is performed using the Levenberg–Marquart method and is of the form:

$$\chi^2 = \sum_{i=0}^{n-1}(f_i - (\dot{\nu}_i(1-\beta_i))^2 + \sum_{i=0}^{n-2}(X_i - \dot{\nu}_i/m)^2 \quad (1)$$

where β_i is the orbital red-shift factor at time t_i, which is a function of the orbital elements, and f_i is the measured barycentric frequency at time t_i, which is the frequency epoch of the search interval i. Each epoch is chosen as the mean exposure-weighted observation time. X_i is the average value of $R^{6/7}$ between t_i and t_{i+1} and R is the BAT rate. The model parameter ν_i is the orbitally corrected frequency at time t_i and $\dot{\nu}_i$ is $(\nu_{i+1} - \nu_i)/(t_{i+1} - t_i)$.

Table 1. Orbital ephemeris for 2S 1553−542.

Orbital period	31.303(27)	days
$T_{\pi/2}$	2457 089.421(19)	days
$a_x \sin i$	201.25(84)	light-seconds
Eccentricity	0.0351(22)	
Longitude of periastron	163.4(35)	degrees
χ^2	66.3 / 38 dof	

The updated orbital model is used in a new search for frequencies and frequency rates recursively until the orbital solution becomes stationary. The final fit resulted in $\chi^2 = 66.3$ with 38 degrees of freedom (dof). The resulting orbital ephemeris of 2S 1553-542 can be found in Table 1. Variability in the pulse profile within the 2-day integration interval contributed to errors in the measured frequency. In addition, changes in the emission beam within the integration interval or systematically throughout the outburst are expected to produce systematic errors in the BAT rates used to model the spin-up. To adjust the errors on the orbital parameters to account for these issues, the errors are increased by 1.35, which results in an orbital fit with a reduced $\chi^2 \sim 1$.

This ephemeris is orbitally phase connected, within 2.7 ± 2.3 d, to the orbit determined in Pahari & Pal (2012) from the 2008 outburst. The spin-down between the 2008 outburst and 2015 outburst is ∼6.5 cycles d^{-1}.

The frequency history, pulsed flux and ephemeris for this source and all other sources monitored by the GBM pulsar monitoring team may be found at the GBM pulsar website.[2]

3.2 Pulse period and profile

To determine the mean pulse period and its uncertainty using the *NuSTAR* observation, we took the barycentred light curve in the wide energy band (3–79 keV) and based on that generated a set of 10^4 trial light curves. For each light curve, we found a pulse period and got a distribution of these trial periods. Individual pulse periods in each light curve were obtained using the EFSEARCH procedure from the FTOOLS package. The mean value of this distribution was taken as the proper pulse period of 2S 1553−542 and the standard deviation as the corresponding 1σ uncertainty (see e.g., Boldin, Tsygankov & Lutovinov 2013).

Following this procedure, we obtained the spin period $P_{\rm spin} = 9.282\,204(2)$ s in the raw data. This corresponds to the intrinsic spin period $P_{\rm spin} = 9.278\,80(3)$ s after the correction for

[1] http://heasarc.gsfc.nasa.gov/docs/swift/results/transients/

[2] http://gammaray.msfc.nasa.gov/gbm/science/pulsars.html

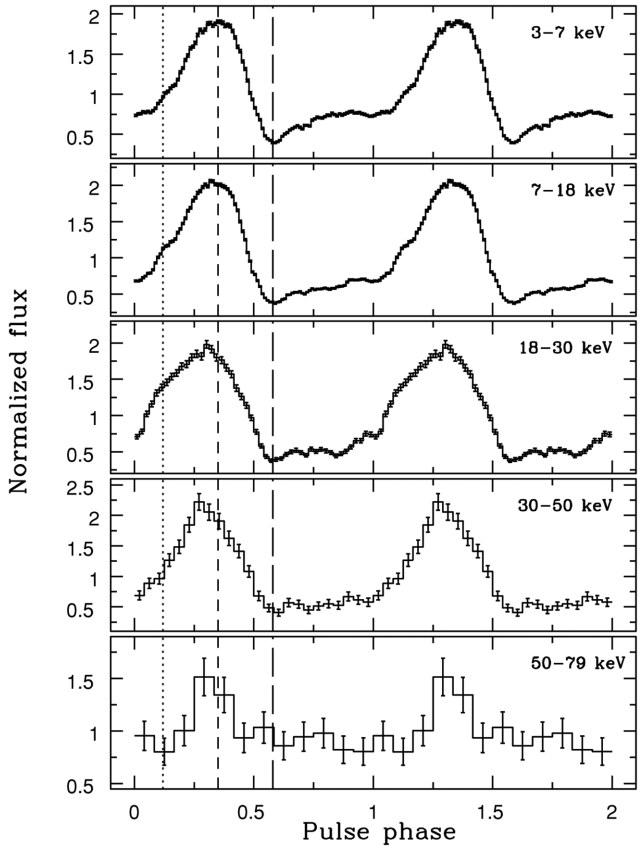

Figure 3. Pulse profiles of 2S 1553−542 as seen by *NuSTAR* in five different energy bands (3–7, 7–18, 18–30, 30–50 and 50–79 keV), normalized by the mean flux in each band (from top to bottom). The profiles are plotted twice for clarity. Vertical lines show the positions of the most prominent features: main maximum (short-dashed line), main minimum (long-dashed line) and energy-dependent wing (dotted line).

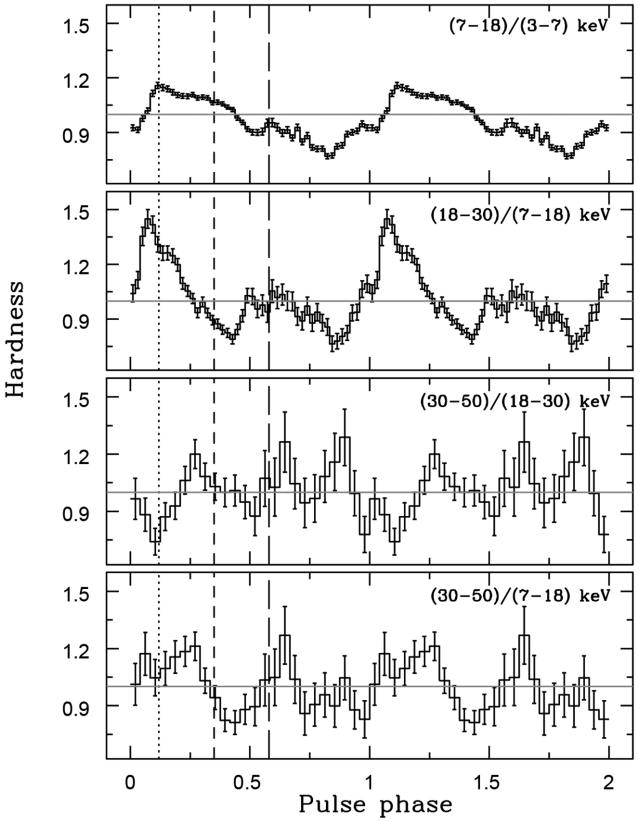

Figure 4. Hardness ratios of 2S 1553−542 pulse profiles in different energy bands (specified in each panel). Vertical lines show the positions of the main features in the pulse profile (see Fig. 3). The grey horizontal line represents the hardness ratio of unity.

the orbital motion using the orbital parameters listed in Section 3.1. An uncertainty for the intrinsic period was calculated using Monte Carlo simulations taking into account uncertainties in the orbital parameters and using standard relations between the pulse period and ephemeris. The spin period from the *NuSTAR* data is shown in the lower panel of Fig. 1 by the asterisk. Interestingly, it is roughly equal to the period when the source was discovered around 40 yr ago. In spite of significant spin-up observed during the outburst episode (see bottom panel of Fig. 1), the constancy of the period over the decades is not surprising due to the rarity of such accretion events and the slow spin-down between them. A very similar picture is seen in many other rarely bursting transient BeXRPs, like 4U 0115+63, V 0332+53, A 0535+262 and others. (See footnote 2)

The pulse profile shape carries useful information about the geometrical properties of the emitting area at the neutron star surface, whereas its dependence on energy reflects the physical properties of the matter–radiation interaction. Following Krivonos et al. (2015), instead of analysing light curves from modules FPMA and FPMB independently, we combined them to get better statistics.

The pulse profile has a single-peak shape with a barely noticeable dependence on energy. Fig. 3 illustrates the evolution of the pulse profiles normalized by the mean flux over five energy bands: 3–7, 7–18, 18–30, 30–50 and 50–79 keV (from top to bottom). Three main features can be distinguished: main maximum, main minimum and energy-dependent wing, appearing in the 18–30 keV energy band. In the figure, these features are shown by a short-dashed line, a long-dashed line and a dotted line, respectively.

Most obviously, the dependence on energy of the pulse profile is illustrated by the hardness ratios shown in Fig. 4. The quite complicated structure of all four ratios is mainly defined by the energy dependence of the main peak. Namely, an additional component appears in the 18–30 keV energy band at phases ∼0.1–0.2 (shown by the dotted line). Interestingly, this component disappears at higher energies. This is clearly seen from the decrease of the hardness ratio below the level of unity in 30–50/18–30 keV in contrast to a significant excess in 18–30/7–18 keV and almost a ratio of unity in 30–50/7–18 keV.

This behaviour is the result of a wave-like structure of the pulse profile shape as a function of energy and is clearly seen in Fig. 5. The dashed line shows the position of the discovered cyclotron line (see Section 3.3). To construct this figure, we used pulse profiles normalized by the mean flux value in each energy band, which were chosen to be the same as in Fig. 6.

The pulsed fraction has a virtually constant value around 60–70 per cent between 3 and 20 keV, whereas at higher energies it shows a non-monotonic dependence on energy (see Fig. 6). The observed behaviour of the pulsed fraction can be interpreted as a local minimum around ∼25 keV superimposed on the gradual increase with energy, typical for the majority of X-ray pulsars (Lutovinov & Tsygankov 2009). Note that only half of all the energy bands here are statistically independent; however, such a representation (equal to a running average) reveals features in the most evident way. At energies above ∼40 keV, one can observe another decrease of the

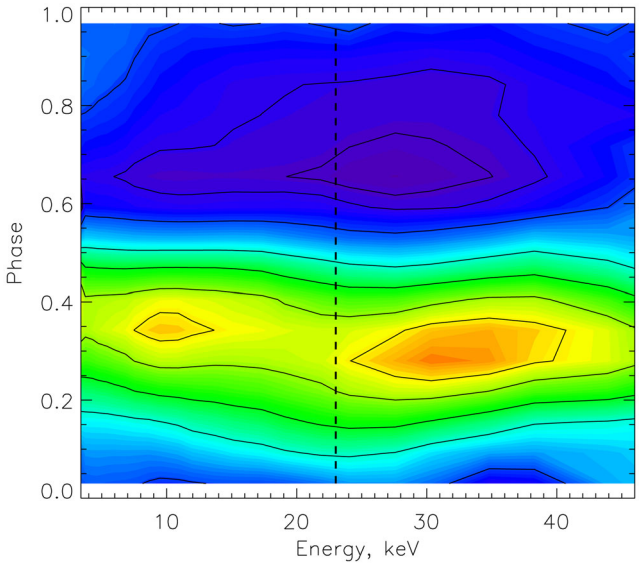

Figure 5. Normalized flux map in energy–pulse phase coordinates. The dashed vertical line shows the position of the cyclotron line centroid energy. Solid contours represent levels of equal normalized flux at 0.45, 0.5, 0.7, 1.1, 1.4, 1.7 and 1.9.

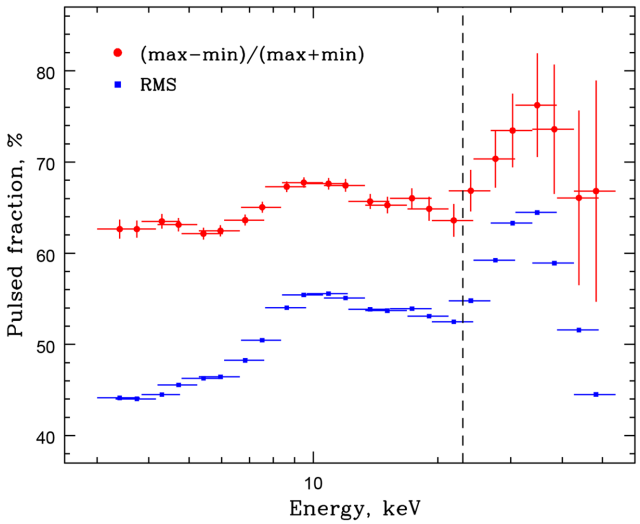

Figure 6. Dependence of the pulsed fraction of 2S 1553−542 on energy obtained using two different approaches (see text for details) based on the *NuSTAR* data. The dashed line shows the position of the CRSF discovered in the source spectrum.

pulsed fraction. A possible physical explanation is an influence of the second harmonics of the cyclotron line, which is expected at these energies. However, as can be seen from Fig. 7, the signal from 2S 1553−542 becomes dominated by the background above 40–50 keV and precise determination of the pulsed fraction depends strongly on the background model. Therefore, the second decrease in the pulsed fraction should be interpreted with caution.

We used two different definitions of the pulsed fraction to avoid any possibly biases due to pulse profile shape or statistics. The standard definition of the pulsed fraction is PF $= (F_{\rm max} - F_{\rm min})/(F_{\rm max} + F_{\rm min})$, where $F_{\rm max}$ and $F_{\rm min}$ are the maximum and minimum fluxes in the pulse profile, respectively. Defined this way, the pulsed fraction is shown by red circles in Fig. 6. Another approach for characterizing the flux variations over the pulse is to use

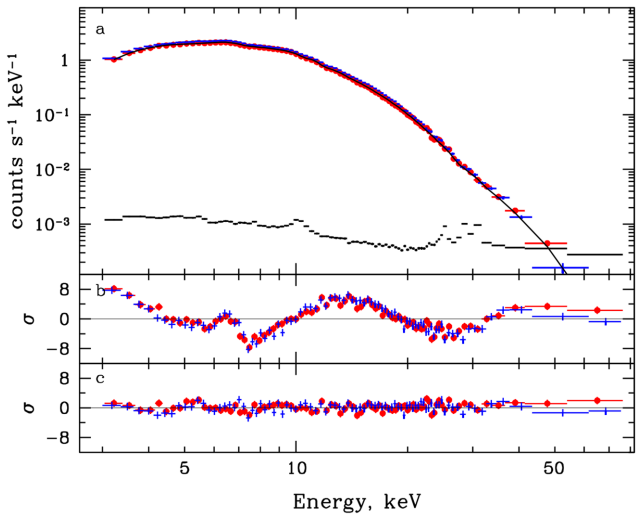

Figure 7. (a) Pulse phase averaged spectrum of 2S 1553−542 obtained with the *NuSTAR* observatory. Red circles and blue crosses correspond to FPMA and FPMB module data, respectively. The black line shows the best fit by the model consisting of PHABS × (BBODYRAD + CUTOFFPL + GAUSS) × CYCLABS. (b) Residuals from the PHABS × CUTOFFPL continuum model. (c) Residuals from the PHABS × (BBODYRAD + CUTOFFPL + GAUSS) × CYCLABS model. Black crosses represent the averaged background level.

the relative root mean square (rms), which can be calculated using the following equation:

$$\mathrm{rms} = \frac{\left(\frac{1}{N}\sum_{i=1}^{N}(P_i - \langle P\rangle)^2\right)^{\frac{1}{2}}}{\langle P\rangle}, \quad (2)$$

where P_i is the background-corrected count rate in a given bin of the pulse profile, $\langle P\rangle$ is the count rate averaged over the pulse period and N is the total number of phase bins in the profile. This definition gives a significantly lower absolute value of the pulsed fraction; however, all features described above have the same form and are located at the same energies.

3.3 Spectral analysis

The main purpose of the *NuSTAR* observations was to search for the cyclotron resonant scattering feature (CRSF) in the source spectrum and to measure its parameters if discovered or to put strict limits on its presence. The *NuSTAR* observatory is perfectly suitable for these purposes, as it uniformly covers the energy range from 3 to 79 keV (without needing to combine different instruments with different response matrixes, like for the *RXTE* and *INTEGRAL* observatories), and it has an unprecedented sensitivity in the energy range 10–50 keV, where most of the known cyclotron absorption lines have been detected (see e.g., Walter et al. 2015 for a recent review of high-mass X-ray binaries). Moreover, the good timing capabilities of *NuSTAR* allow us to perform the same analysis also for pulse phase resolved spectra, as sometimes cyclotron features are detected only for limited pulse phase intervals and they are not seen in the pulse-averaged spectra. In the following spectral analysis of the source emission, we used a fixed hydrogen column density of 2.3×10^{22} cm^{-2} (Lutovinov et al. 2015b).

3.3.1 *Pulse phase averaged spectroscopy*

In general, the spectrum of 2S 1553−542 has a shape that is typical for accreting X-ray pulsars and it demonstrates an exponential

cut-off at high energies (Fig. 7a). Therefore, we initially approximated it with the cut-off power-law model (PHABS × CUTOFFPL in the XSPEC package). The results of this fitting give an unacceptable value of $\chi^2 = 3432.1$ for 1303 dof; the corresponding residuals are shown in Fig. 7(b). The source and background spectra from both FPMA and FPMB were used for simultaneous fitting, without co-adding. To take into account the uncertainty in their calibrations, a cross-calibration constant between the modules was added to any spectral model used. From this figure, two peculiarities are clearly seen in the spectrum: an excess at low energies and a depression between 20 and 30 keV. Including in the model an additional blackbody component (the BBODYRAD model in the XSPEC package) with a temperature of about 1 keV significantly improves the fit, but the value of $\chi^2 = 1726.7$ for 1300 dof is still quite large and associated with a deficit of photons between 20 and 30 keV. Therefore, for the next step, we introduced into the model an absorption component in the form of the CYCLABS model in the XSPEC package. It led to the following improvement of the χ^2 value to 1306.5 for 1297 dof. The corresponding residuals are shown in Fig. 7(c). The line centroid energy is ≃23.5 keV.

Notice that the appearance of this feature is not a consequence of the combination of some particular continuum models. We investigated several other spectral models or their combinations to describe the continuum: POWERLAW × HIGHECUT, BBODYRAD + BKNPOWER, COMPTT, BBODYRAD + COMPTT, COMPTT + COMPTT. We found that (1) all of them approximate it insufficiently well and (2) residuals for all of them demonstrate a prominent absorption-like feature in the 20–30 keV energy range. Thus, we can conclude that this absorption feature is real. We interpret this feature as a cyclotron absorption line. Usually, two different models, CYCLABS and GABS in the XSPEC package, are used to describe such a feature. Both models adequately approximate an absorption line, but the cyclotron line energy derived from the CYCLABS model is systematically lower (by ∼1–3 keV) than the energy derived from the GABS model (see e.g., Mihara 1995; Tsygankov, Krivonos & Lutovinov 2012; Lutovinov et al. 2015a).

Additionally, the prominent emission feature near 6.4 keV is clearly detected in the source spectrum. This feature is associated with the fluorescent iron emission line and often observed in spectra of BeXRPs. To take it into account, we added to the model a corresponding component in the Gaussian form.

Thus, the final spectral models that were used for the approximation of the 2S 1553−542 spectrum in the XSPEC package are: PHABS × (BBODYRAD + CUTOFFPL + GAUSS) × CYCLABS (model I) and PHABS × (BBODYRAD + CUTOFFPL + GAUSS) × GABS (model II). Their best-fitting parameters are summarized in Table 2. Note that the normalization of the blackbody component is proportional to the surface area and depends on the radius of the emission region R_{bb} and distance to the source d as $A = (R_{bb}/d_{10})^2$, where R_{bb} is expressed in kilometres and d_{10} in units of 10 kpc.

We are not able to detect the second harmonics of the cyclotron line with the existing data due to the instrumental response drop-off at high energies and high level of the background (see Fig. 7a). The 3σ upper limit on the optical depth of the second harmonics is 1.4, assuming its width is 10 keV. More observational data or other instruments are needed to make a final conclusion about its presence in the spectrum.

3.3.2 *Pulse phase resolved spectroscopy*

As was mentioned above, the spectra of X-ray pulsars can vary significantly over the pulse. The observed variations of spectral parameters can give information about changes of the physical conditions or parameters of the emission regions near the neutron star. To study their evolution over the pulse period for 2S 1553−542, we performed pulse phase resolved spectroscopy. The spin period was divided into 10 equal phase bins. The pulse profile has a more or less smooth shape (Fig. 3); therefore, such a division allows us to obtain a good statistic for each spectrum and to trace the evolution of the spectral parameters well.

Table 2. Best-fitting parameters of the 2S 1553−542 spectrum.

Parameter	Model I	Model II
Constant	1.015 ± 0.002	1.015 ± 0.002
N_H, 10^{22} cm^{-2}	2.3	2.3
kT_{BB}, keV	0.94 ± 0.02	0.94 ± 0.02
A_{BB}[a]	18.7 ± 1.3	19.54 ± 1.3
Photon index	-0.53 ± 0.06	-0.66 ± 0.08
E_{cut}, keV	5.59 ± 0.17	5.06 ± 0.10
τ_{cycl}	0.60 ± 0.05	8.28 ± 1.26
E_{cycl}, keV	23.46 ± 0.35	27.34 ± 0.38
σ_{cycl}, keV	10.8 ± 1.0	6.44 ± 0.45
E_{Fe}, keV	6.45 ± 0.04	6.45 ± 0.04
σ_{Fe}, keV	0.41 ± 0.06	0.42 ± 0.06
EW, eV	87 ± 9	89 ± 10
Flux (3–79 keV)[b]	1.025 ± 0.016	1.025 ± 0.016
Flux (3–20 keV)[b]	0.880 ± 0.017	0.880 ± 0.017
χ^2 (dof)	1306.5 (1297)	1301.5 (1297)

[a]Normalization of the blackbody component (see text); [b]units of 10^{-9} erg s^{-1} cm^{-2}.

To describe the phase-resolved spectra, we used the same spectral model as for the analysis of the averaged spectrum (with the CYCLABS prescription for the cyclotron line; model I). Note that the width of the cyclotron line cannot be firmly determined in some phase bins due to insufficient photon statistics. Therefore, its value was fixed at 8 keV – the value that was measured in phase bins near the pulse maximum with the better statistics.

The results of the pulse phase-resolved spectroscopy are shown in Fig. 8. The average pulse profile of 2S 1553−542 across the entire *NuSTAR* energy range is presented in each panel to visualize better the variations of spectral parameters with the phase. The photon index varies quite significantly (from −2 to 0) whereas the cut-off energy is less variable, staying in the range between 4 and 6 keV. We can mention also a possible tentative correlation between these parameters. The temperature of the blackbody component is around ≃1 keV and is quite stable over the pulse with some variations from ∼1.1 to ∼0.7 keV in the first three bins.

Variations of the cyclotron line energy and the line depth are the most interesting and important for us, as both of them change significantly over the pulse. In particular, the line centroid energy has a minimum ($E_{cycl} \simeq 21$ keV) near the pulse profile maximum, whereas the line depth has a maximum near this phase. In general, the line energy E_{cycl} varies between ≃21 and ≃27 keV (using the CYCLABS model for the cyclotron line), and this is the main reason for the significant broadening of the line measured in the averaged spectrum (∼11 keV). Note that the described behaviour of the cyclotron line parameters over the pulse is very similar to that observed for the well-studied BeXRP V 0332+53. This object had nearly the same luminosity $L \simeq 6 \times 10^{37}$ erg s^{-1} (Lutovinov et al. 2015a). From another side, this behaviour is the opposite to what was observed for sub-critical pulsars due to their different beaming properties [see e.g., Klochkov et al. (2008) for the X-ray pulsar Her X-1].

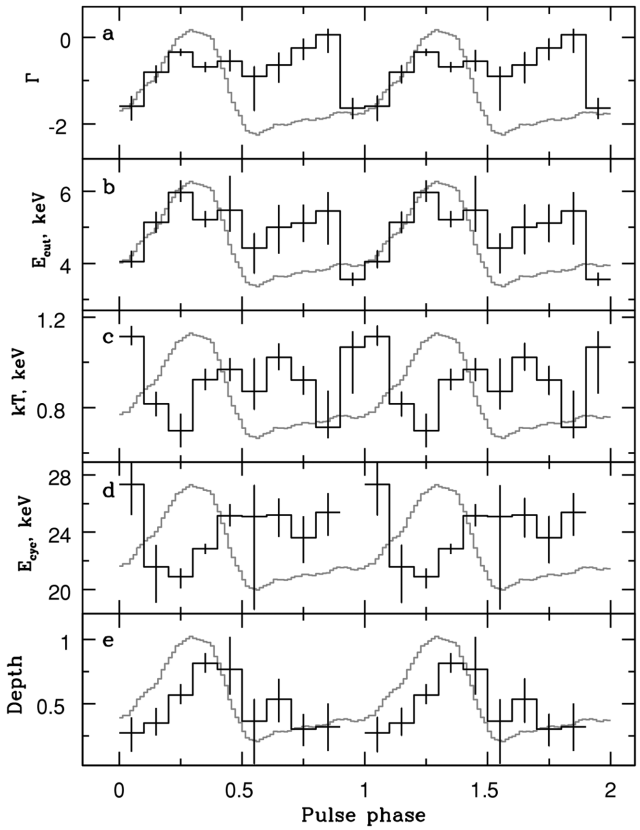

Figure 8. Spectral parameters of the best-fitting model (model I, see text) as a function of pulse phase. The black histogram in the panels represents: (a) photon index, (b) cut-off energy, (c) blackbody temperature, (d) cyclotron line energy and (e) cyclotron line depth. The grey line in each panel shows the pulse profile in a wide energy range. The cyclotron line is not detected in the 10th bin.

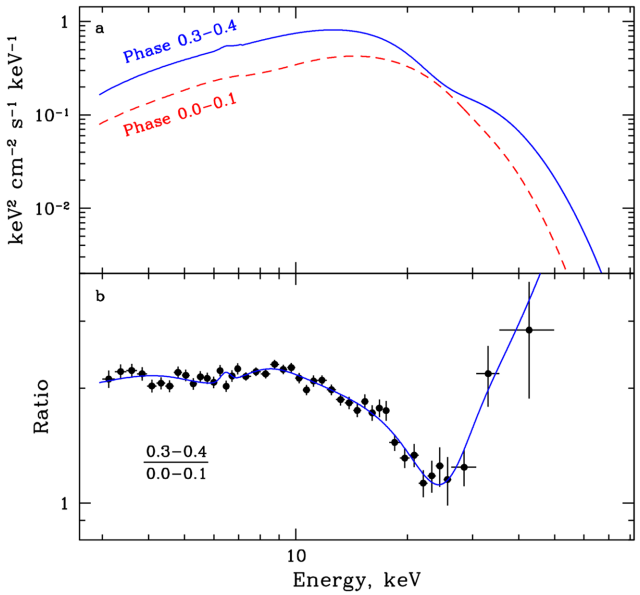

Figure 9. (a) Best-fitting spectral models for two different phase bins. Red dashed line and blue solid line represent phases 0.0–0.1 and 0.3–0.4, respectively. Their ratio is shown in panel (b). A prominent absorption-like feature is seen between 20 and 30 keV.

To demonstrate that the observed spectral variations are real, we show the ratio of two spectra obtained in the first (minimal line depth) and fourth (maximal line depth) phase bins in Fig. 9. The upper panel demonstrates corresponding models for these spectra. The ratio of the observed spectra is shown in the bottom panel with filled circles. The solid line in this panel represents the ratio of the corresponding models. A strong absorption-like feature, caused by the difference in line depths for these phase bins, is clearly seen in this figure between 20 and 30 keV.

The contribution of different continuum components (blackbody and power-law with cut-off) to the total source luminosity demonstrates a variability of their ratio over the pulse. In particular, the blackbody flux remains virtually constant at the level of $\sim 9 \times 10^{-11}$ erg s^{-1} cm^{-2}, whereas the power-law flux dominates at all phases and determines the overall pulse profile shape. The contribution of the blackbody emission to the total flux varies between ∼5 and ∼15 per cent. Using an estimation of the distance to the source $d \sim 20$ kpc (see Section 4), the measured blackbody flux corresponds to an emitting area with a radius of $R \sim 9$ km. This value is comparable with the neutron star size, which means that the blackbody emission can emerge from the neutron star atmosphere heated by the intercepted emission from the accretion column (Poutanen et al. 2013). Thus, the big radius of the illuminated surface area of the neutron star can explain the virtual constancy of the blackbody emission component over the pulse. This hypothesis could be verified by a set of observations of 2S 1553−542 at different luminosities and, hence, with different illuminated areas on the neutron star.

4 DISCUSSION

In this work, we presented a detailed spectral and temporal analysis of the emission from the poorly studied BeXRP 2S 1553−542 using the *NuSTAR* data collected during the presumably type II outburst in 2015. The energy spectrum of the source cannot be fitted satisfactorily with any simple continuum model but requires inclusion of the absorption feature centred at ∼23.5 keV.

This absorption component has a clear physical meaning and represents the cyclotron absorption line known to be the main evidence for the strong magnetic field on the neutron star surface (Gnedin & Sunyaev 1974). The absorption line in the 2S 1553−542 spectrum can be fitted either by the Gaussian (GABS model) or the Lorentzian (CYCLABS model) profiles with approximately the same quality. The line energy (≃27.3 keV for GABS and ≃23.5 keV for CYCLABS) corresponds to the magnetic field strength at the neutron star surface, $B \sim 3 \times 10^{12}$ G, after the correction for the gravitational red shift.

The existence of the cyclotron feature is confirmed not only by the spectral fitting, but also by the temporal properties of the source. In particular, the dependence of the pulsed fraction on the energy has a broad feature (local decrease) around 23 keV (see Fig. 6), which coincides with the position of the CRSF in the source spectrum. Such non-monotonic dependencies of the pulsed fraction on energy have been observed for several X-ray pulsars with a cyclotron line in their spectra (Lutovinov & Tsygankov 2009; Ferrigno et al. 2009) and they have even been proposed as a tool to search for CRSFs.

Further evidence for the cyclotron absorption feature comes from the behaviour of the pulse profile with energy. A phase lag around the spectral feature can be clearly seen in Figs 3 and 5, expressed in a wave-like structure near 20–30 keV. Such behaviour has been shown to be typical for a few other transient BeXRPs (Tsygankov et al. 2006, 2007; Iyer et al. 2015) and can be explained by a natural

assumption of an energy-dependent beaming of the radiation from the emitting region (Ferrigno et al. 2011; Schönherr et al. 2014).

Knowing the magnetic field strength gives us an opportunity to estimate the absolute value of the mass accretion rate needed to provide the spin-up rate measured by *Fermi*/GBM at the moment of our *NuSTAR* observation $\dot{P} = -(7.5 \pm 0.9) \times 10^{-10}$ s s^{-1}. For that, we used the accretion torque theories developed by different authors (Ghosh & Lamb 1979; Wang 1995; Kluźniak & Rappaport 2007). These models explain the observed spin-up/-down rate as a function of the neutron star parameters and they depend on the physics of the accretion disc–magnetosphere interaction. For our calculations, we used the neutron star magnetic dipole moment $\mu = 1.5 \times 10^{30}$ G cm^3, derived from the measured value of the magnetic field strength, and 1.4 $M_\odot$ and 10 km as the neutron star mass and radius, respectively, keeping the mass accretion rate as a free parameter.

Type II outbursts in BeXRPs are usually accompanied by the formation of a temporary accretion disc around the neutron star [see e.g., (Reig 2011) and references therein], revealing itself in a strong spin-up rate and the properties of the noise power spectrum (Revnivtsev et al. 2009). Therefore, as a first approximation, we used equation (15) from Ghosh & Lamb (1979) to estimate the bolometric luminosity $L = (7.6 \pm 0.9) \times 10^{37}$ erg s^{-1} needed to support the measured spin-up rate. Given the flux from 2S 1553−542 during the *NuSTAR* observation $F = 1.05 \times 10^{-9}$ erg s^{-1} cm^{-2}, the distance to the system can be estimated as $d \sim 22$ kpc.

The torque model by Ghosh & Lamb (1979) is not the only one developed for disc accretion. In all these models, the total torque can be expressed in the form $N_{\rm tot} = n(\omega_s)N_{\rm acc}$. The only parameter of the dimensionless angular momentum $n(\omega_s)$ is the so-called fastness parameter $\omega_s = (r_{\rm m}/r_{\rm co})^{3/2}$, where $r_{\rm m}$ and $r_{\rm co}$ are the magnetospheric and co-rotation radii, respectively. We used different prescriptions for the dimensionless angular momentum $n(\omega_s)$, which describes the physical properties of the interaction of the accretion disc with the magnetosphere. In particular, utilizing approaches from Kluźniak & Rappaport (2007) and Wang (1995), we got distances $d \sim 17$ kpc and $d \sim 22$ kpc, respectively. That the dispersion of the distances derived from different models is not large, is due to the source being far from spin equilibrium, where the difference in the above-mentioned models is maximal (see e.g., fig. 2 from Parfrey, Spitkovsky & Beloborodov 2015).

The radius of the magnetosphere in these models is assumed to be a fraction of the Alfvén radius $r_{\rm m} = \xi r_{\rm A}$. In the calculations above, we assumed the parameter $\xi = 0.5$; however, its exact value is not known and is supposed to be between 0.5 and 0.7 [see e.g., Parfrey et al. (2015) and references therein]. To estimate a possible influence of this parameter for our results, we recalculated distances with $\xi = 0.7$. This affected the derived values very insignificantly, shifting the distance estimations based on the models by Ghosh & Lamb (1979) and Wang (1995) to ∼24 and ∼21 kpc, respectively. These estimations make 2S 1553−542 one of the most distant high-mass X-ray binaries in the Galaxy (Lutovinov et al. 2013), putting it on the opposite side of the Milky Way. Importantly, the distance estimations based on the temporal properties of X-ray pulsars have quite large systematic uncertainties (of the order of 15–20 per cent) due to model dependency, the unknown efficiency of the accretion and the effects of possible emission beaming; therefore, they should be considered with caution. Nevertheless, a large distance to the source (>15 kpc) is estimated from the optical data as well (Lutovinov et al. 2015b).

The dispersion of the estimated distance values can be considered as a systematic uncertainty of this method. It is interesting to note that, if our estimations of distance (20 ± 4 kpc) are correct, then 2S 1553−542 exceeds the so-called critical luminosity above which the accretion column begins to grow above the neutron star surface (Basko & Sunyaev 1976). The value of the critical luminosity as well as conditions for the growth of the accretion column are still under debate and depend on the physical models [see e.g., Mushtukov et al. (2015) and references therein]. A set of observations in different intensity states during the outburst is needed to verify this hypothesis by, e.g., observing the anti-correlation between the cyclotron energy and source luminosity, as seen for at least one bright transient X-ray pulsar V 0332+53 (Mihara, Makishima & Nagase 1998; Tsygankov et al. 2006; Tsygankov, Lutovinov & Serber 2010). The presence of such an anti-correlation for another similar source, 4U 0115+63, is still under debate (Nakajima et al. 2006; Tsygankov et al. 2007; Müller et al. 2013; Boldin et al. 2013).

5 CONCLUSION

The recent outburst from BeXRP 2S 1553−542 was only the third transient event when the source was in the view of X-ray instruments. Thanks to the wide energy coverage and high sensitivity of *NuSTAR*, we were able to discover a cyclotron absorption line with centroid energy $E_{\rm cyc} = 23.5 \pm 0.4$ keV, corresponding to the neutron star magnetic field strength $B \sim 3 \times 10^{12}$ G, typical for known X-ray pulsars (Walter et al. 2015). The presence of the cyclotron line in the source spectrum is also supported by the behaviour of the pulse profile and pulsed fraction with energy.

The pulse phase resolved spectroscopy revealed significant variations of the cyclotron line parameters over the pulse. In particular, the line centroid energy anti-correlates with the intensity, whereas the line depth shows a correlation.

Thanks to the *Fermi*/GBM data, we were able to improve substantially the orbital parameters of the system. The intrinsic spin period and its evolution observed by *Fermi*/GBM and *NuSTAR* during the current outburst are similar to those measured by the *RXTE* observatory during the previous outburst (Pahari & Pal 2012). The virtual constancy of the period since the source was discovered in 1975 and a significant spin-up observed during both outbursts (up to $\dot{P} \sim -10^{-9}$ s s^{-1}) imply the action of deceleration torques between outbursts. Taking into account the last measured value of the pulse period during the previous outburst (Pahari & Pal 2012) and its first measured value during the current outburst (Fig. 1), we can estimate roughly the spin-down between the 2007 and 2015 outbursts as $\dot{P} \sim (3\text{–}4) \times 10^{-11}$ s s^{-1}. This value is more than an order of magnitude lower than the spin-up during the outbursts and comparable with the spin-down observed between outbursts in other BeXRBs (see e.g., Postnov et al. 2015).

Knowing the magnetic field and spin-up rate allowed us to estimate the distance to the system $d = 20 \pm 4$ kpc using the standard accretion torque models. Such a large distance agrees well with the fact that the optical counterpart has not directly been detected so far.

ACKNOWLEDGEMENTS

This research made use of data obtained with *NuSTAR*, a project led by Caltech, funded by NASA and managed by NASA/JPL, and it utilized the NUSTARDAS software package, jointly developed by the ASDC (Italy) and Caltech (USA). This research also used *Chandra* data provided by the Chandra X-ray Center. The publication uses software provided by the Chandra X-ray Center (CXC) in the application package CIAO. ST, AL and SM acknowledge support from

the Russian Science Foundation (grant 14-12-01287). JP thanks the Academy of Finland for financial support (grant 268740). Partial support comes from the EU COST Action MP1304 NewCompStar.

REFERENCES

An H. et al., 2014, SPIE, 9144, 91441Q
Basko M. M., Sunyaev R. A., 1976, MNRAS, 175, 395
Boldin P. A., Tsygankov S. S., Lutovinov A. A., 2013, AstL, 39, 375
Deeter J. E., Boynton P. E., Pravdo S. H., 1981, ApJ, 247, 1003
Dickey J., Lockman F., 1990, ARA&A, 28, 215
Ferrigno C., Becker P. A., Segreto A., Mineo T., Santangelo A., 2009, A&A, 498, 825
Ferrigno C., Falanga M., Bozzo E., Becker P. A., Klochkov D., Santangelo A., 2011, A&A, 532, A76
Finger M. H., Bildsten L., Chakrabarty D., Prince T. A., Scott D. M., Wilson C. A., Wilson R. B., Zhang S. N., 1999, ApJ, 517, 449
Ghosh P., Lamb F. K., 1979, ApJ, 234, 296
Gnedin I. N., Sunyaev R. A., 1974, A&A, 36, 379
Harrison F. A. et al., 2013, ApJ, 770, 103
Iyer N., Mukherjee D., Dewangan G. C., Bhattacharya D., Seetha S., 2015, MNRAS, 454, 741
Jenke P. A., Finger M. H., Wilson-Hodge C. A., Camero-Arranz A., 2012, ApJ, 759, 124
Kalberla P., Burton W., Hartmann D., Arnal E., Bajaja E., Morras R., Pöppel W., 2005, A&A, 440, 775
Kelley R. L., Ayasli S., Rappaport S., 1982, IAUC, 3667, 3
Kelley R. L., Rappaport S., Ayasli S., 1983, ApJ, 274, 765
Klochkov D. et al., 2008, A&A, 482, 907
Kluźniak W., Rappaport S., 2007, ApJ, 671, 1990
Krimm H. A. et al., 2007, ATel, 1345, 1
Krimm H. A. et al., 2013, ApJS, 209, 14
Krivonos R. A. et al., 2015, ApJ, 809, 140
Lutovinov A. A., Tsygankov S. S., 2009, AstL, 35, 433
Lutovinov A. A., Revnivtsev M. G., Tsygankov S. S., Krivonos R. A., 2013, MNRAS, 431, 327
Lutovinov A. A., Tsygankov S. S., Suleimanov V. F., Mushtukov A. A., Doroshenko V., Nagirner D. I., Poutanen J., 2015a, MNRAS, 448, 2175
Lutovinov A. et al., 2015b, MNRAS, submitted
Meegan C. et al., 2009, ApJ, 702, 791
Mihara T., 1995, PhD thesis, Dept. of Physics, Univ. of Tokyo
Mihara T., Makishima K., Nagase F., 1998, AdSpR, 22, 987
Müller S. et al., 2013, A&A, 551, A6
Mushtukov A. A., Suleimanov V. F., Tsygankov S. S., Poutanen J., 2015, MNRAS, 447, 1847
Nakajima M., Mihara T., Makishima K., Niko H., 2006, ApJ, 646, 1125
Pahari M., Pal S., 2012, MNRAS, 423, 3352
Parfrey K., Spitkovsky A., Beloborodov A. M., 2015, preprint (arXiv:1507.08627)
Postnov K. A., Mironov A. I., Lutovinov A. A., Shakura N. I., Kochetkova E. A., Tsygankov S. S., 2015, MNRAS, 446, 1013
Poutanen J., Mushtukov A. A., Suleimanov V. F., Tsygankov S. S., Nagirner D. I., Doroshenko V., Lutovinov A. A., 2013, ApJ, 777, 115
Rappaport S., Joss P. C., 1977, Nature, 266, 123
Reig P., 2011, Ap&SS, 332, 1
Revnivtsev M., Churazov E., Postnov K., Tsygankov S., 2009, A&A, 507, 1211
Schönherr G. et al., 2014, A&A, 564, L8
Standish E. M., Jr, 1990, A&A, 233, 252
Sugizaki M. et al., 2015, ATel, 7018, 1
Tsygankov S. S., Lutovinov A. A., Churazov E. M., Sunyaev R. A., 2006, MNRAS, 371, 19
Tsygankov S. S., Lutovinov A. A., Churazov E. M., Sunyaev R. A., 2007, AstL, 33, 368
Tsygankov S. S., Lutovinov A. A., Serber A. V., 2010, MNRAS, 401, 1628
Tsygankov S. S., Krivonos R. A., Lutovinov A. A., 2012, MNRAS, 421, 2407
Walter F., 1976, IAUC, 2959, 2
Walter R., Lutovinov A. A., Bozzo E., Tsygankov S. S., 2015, A&AR, 23, 2
Wang Y.-M., 1995, ApJ, 449, L153
Wik D. R. et al., 2014, ApJ, 792, 48

This paper has been typeset from a TEX/LATEX file prepared by the author.